327. Surface Micromachined Comb Drive with Superior Stability for Application as an Actuator

Yanxia Zhang and M.Kahrizi
Concordia University, Montreal, QC, H3G 1M8, CANADA
E-mail: *mojtaba@ece.concordia.ca*

(Received 13 February 2008; accepted 17 March 2008)

Abstract. This paper presents results of ongoing research on fundamental issues related to comb drive, including mechanical and electrical properties. Attention is mostly focused on the case when comb drive is used as a power source with a cantilever beam attached to the moving plate. FEM simulations are carried out to show the resonant behaviour of balanced and unbalanced comb drive. Fringing effect, which helps to actuate the comb drive, is modeled. Different measurement approaches in frequency domain are discussed. Theoretical formulas are derived and analyzed. In this work we designed and fabricated both balanced and unbalanced comb drives using MUMPs (Multi-user MEMS Processes) technology. Balanced comb drives exhibit superior stability both in SEM observations and spectrum analysis. Formulas governing the spectrum are experimentally verified by mixing frequency measurements.

Introduction

There exist a variety of situations when a microsized power source is required to actuate a micromechanism, supplying either linear or rotating motion. Previously demonstrated micromotors might be used if a means for low starting voltage, high rotating speed and lower friction are achieved [1,2]. An alternative approach is an electrostatic comb drive with folded springs, which is widely used because it offers large linear deflection range and high stiffness ratio between vertical and lateral motions.

The comb drive has direct application as a power source for micromachined mechanisms such as optical and electrical microswitches, micropositioners or any other microsized devices that require mechanical power [3]. In most cases where comb drive is used as a power source, a cantilever beam is attached to the moving plate, perpendicular to the length of folded springs, such as the surface micromachined microengine [3], integrated gear linkages [4] and the vertical micromirror arrays for optical switching [5], as shown in Fig. 1. However, in these cases, the asymmetry of the comb drive may lead to system failure due to rotational motion. Even though several successful system operations were demonstrated [3-5] and detailed theoretical analysis, simulations as well as experimental results of standard comb drive were reported [6-8], no research is carried out on the behaviour of comb drive with an attached cantilever beam.

In this work, both mechanical and electrical properties of comb drive are addressed, special issues of comb drive with attached beam are discussed. Unbalanced and balanced comb drives are fabricated and tested. Theoretical formulas governing the spectrum are experimentally verified. In both SEM observations and spectrum analysis, balanced comb drives demonstrate superior stability over unbalanced comb drives.

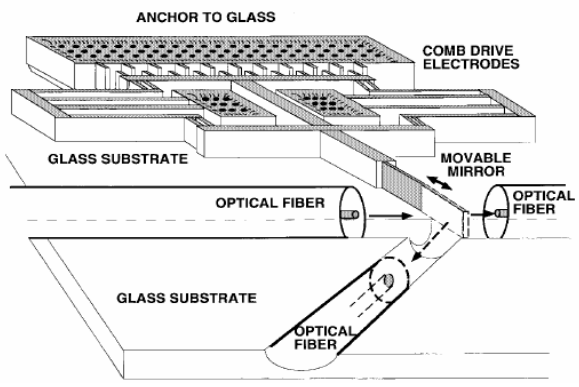

Fig. 1. Optical switch driven by electrostatic comb drive [5]

Mechanical and Electrical Properties

Common feature of comb drive used as power source is that its resonant mode should be linear. The designers should explicitly choose mechanical geometries that preclude rotational motion. The folded-beam suspension can effectively suppress vertical vibration and rotational motion by high stiffness ratios. However, when a cantilever beam is attached to the moving plate at one side, perpendicularly to the length of the folded springs, the geometry is not symmetric and the system is susceptible to rotational motions. Deliberate considerations are necessary to maintain the system rotational equilibrium, in other words, to maintain torque balance. The simplest design is "balanced comb drive", attaching a beam with the same shape and mass on the other side.

For balanced comb drive, the first three resonant modes are shown in Fig. 2. The lateral resonant frequency can be calculated using Rayleigh's energy method [6,8]:

$$f_0 = \frac{1}{2\pi}\left[\frac{k_x}{M_{eff}}\right]^{\frac{1}{2}} = \frac{1}{2\pi}\left[\frac{2Eh(W/L)^3}{M_p + 1/4 M_t + 12/35 M_b}\right]^{\frac{1}{2}} \quad (1)$$

where M_p is the shuttle mass, M_t is the total combined mass of folding trusses; M_b is the total combined mass of the suspending beams.

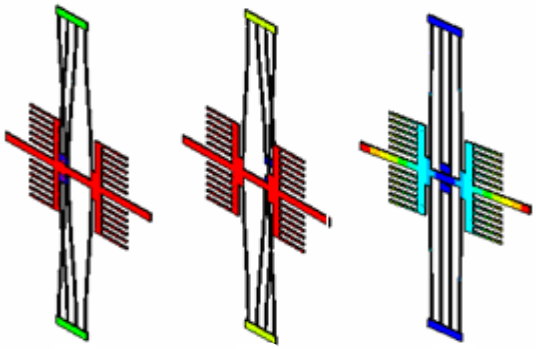

(*a*) (*b*) (*c*)

Fig. 2. Displacement contour plots of the first three resonant modes of the balanced design, a) lateral resonant mode; b) vertical resonant mode; and c) rotational resonant mode

The comb drive uses electrostatic attraction to provide movement. The capacitance between the fixed fingers and movable fingers can be modeled by the parallel plate capacitor. In general, fringing effect for parallel plate capacitor may be neglected as long as both the width and height of the capacitor are significantly larger than the separation, a condition that is not met here. In order to illuminate electrical field distribution and take the fringing effect into account, FEM simulation is carried out and the results are provided in Fig.3

3-D model of two sets of fingers, appearing as solid lines in Fig 3, surrounded by a 10-μm layer of air is built in MEMSPro. The structure profile is 2-μm-thick, 3-μm -wide and 40-μm-long fingers with 3-μm gap in between, 20-μm engagement and 2-μm offset above the 0.6-μm shielding. Fig. 3.a presents the front view of the electrical field vector plot when the fixed fingers (left) are biased at 10 Volts and the movable fingers (right) are connected to the ground. The electrical field and the negative charge on the movable structure yield an attractive force, which is the mechanism of the lateral displacement. The cross-section view is illustrated in Fig. 3.b. The downward electrical field and the negative charge on the movable fingers produce an upward electrostatic force, which is the mechanism of vertical levitation.

The levitation may cause the attached beam to deflect downward. If there is a pawl-ratchet mechanism at the other end of the beam, it might lead to disengagement. It is essential that both structures remain in the same plane. Special care should be taken to prevent the vertical levitation [7,9].

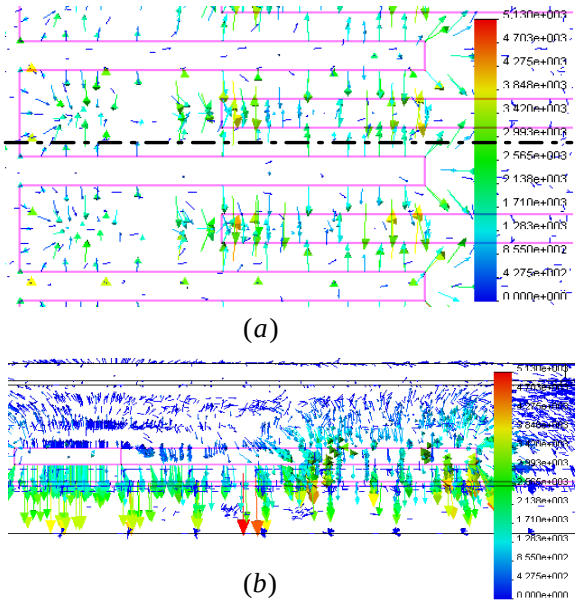

(*a*)

(*b*)

Fig. 3. The electrical field vector plot simulated using COSMOSEMS: a) front view; b) cross-section view

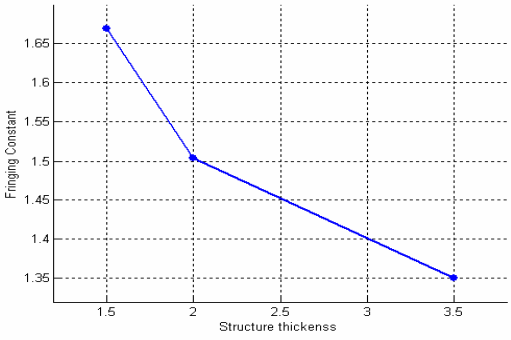

Fig. 4. The variation of fringing constant versus structure thickness

The fringing effect is clearly shown in Fig.3 by the electrical field distribution outside the finger engagement. If we define ξ as a coefficient that models additional

capacitance due to fringing, equal to the actual capacitance over the theoretical capacitance, then the simulation results in $\xi = 1.504$. The variation of the fringing constant versus the thickness of the polysilicon layer is shown in Fig.4.

Fabrication

The device fabrication is provided by Cronos Integrated Microsystems, Inc. through Canadian Microelectronic Corporation (CMC). The Multi-User MEMS Process, known as MUMPs technology, is a triple polysilicon, single metal surface micromachining process with silicon oxide (PSG) as the sacrificial material, and silicon nitride for electrical isolation from the highly conductive substrate [10]. Both balanced and unbalanced comb drives, with or without rack and pinion engagement, were fabricated with poly1 as the structural layer. Successful device release is achieved by HF sacrificial etching and supercritical carbon dioxide drying. Fig. 5.a presents one unbalanced comb drive with a beam attached on the right to transform linear lateral motion to rotational motion through rack and pinion engagement. The initial rotation of the pinion is due to fluid force in HF release process; Fig. 5.b shows a balanced comb drive with attached cantilever beams at both sides.

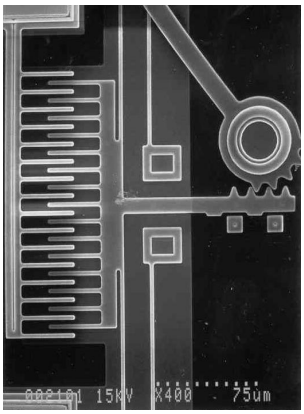

(*a*)

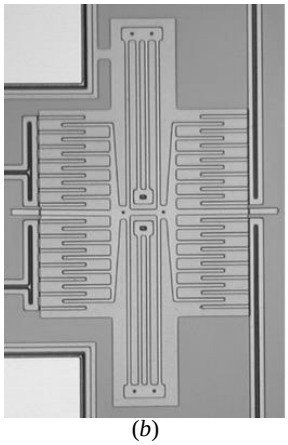

(*b*)

Fig. 5. Unbalanced (a) and balanced (b) comb drives used as power sources

Measurement Methods

Fig. 6. a plots the schematic of mixing frequency measurement in atmospheric air conditions. The series LCR equivalent circuit of the comb drive is in parallel with a probe-to-probe parasitic capacitance, as shown in Fig.6.b. The current spectrum at sense electrode in Fig.6.c illustrates that the motional current at ω_d is amplitude modulated by the carrier to frequencies at $\omega_c - \omega_d$ and $\omega_c + \omega_d$, successfully separated from the parasitic feedthrough. The output is amplified by a transmittance amplifier, then entered into the "Demod" box, where the signal passes a bandpass filter (Fig.6.c) to remove frequency component at ω_d, and then demodulated by a balanced Gilbert cell multiplier. Finally, the demodulated spectrum (Fig.6.d) enters into a low-pass filter, generating a signal near ω_0, which is suitable for input to spectrum analyzer.

Under the bias configuration of Fig.6.a, the electrostatic force, including fringing effect, can be calculated as:

$$F_x = \frac{\xi}{2}\frac{\partial C}{\partial x}(V_p + V_d \sin\omega_d t + V_c \sin\omega_c t)^2 \qquad (2)$$

Using the principle of superposition, the steady-state response of the forced oscillation system equation

$M \cdot d^2x/dt^2 + c \cdot dx/dt + k_x x = F_x(t)$ is:

$$x(t) = \frac{\xi}{2k_x}\frac{\partial C}{\partial x}(V_p{}^2 + \frac{1}{2}V_d{}^2\frac{1}{2}V_c{}^2) + \frac{\xi\frac{\partial C}{\partial x}V_pV_d\sin(\omega_d t - \phi_1)}{\sqrt{\left(k_x - M\omega_d{}^2\right)^2 + c^2\omega_d{}^2}}$$

$$+\frac{\xi\frac{\partial C}{\partial x}V_pV_c\sin(\omega_c t - \phi_2)}{\sqrt{\left(k_x - M\omega_c{}^2\right)^2 + c^2\omega_c{}^2}} + \frac{\xi\frac{\partial C}{\partial x}V_cV_d\cos(\omega_c t - \omega_d t - \phi_5)}{2\sqrt{\left(k_x - M(\omega_c - \omega_d)^2\right)^2 + c^2(\omega_c - \omega_d)^2}}$$

$$-\frac{\xi\frac{\partial C}{\partial x}V_c{}^2\cos(2\omega_c t - \phi_3)}{4\sqrt{\left(k_x - 4M\omega_c{}^2\right)^2 + 4c^2\omega_c{}^2}} - \frac{\xi\frac{\partial C}{\partial x}V_d{}^2\cos(2\omega_d t - \phi_3)}{4\sqrt{\left(k_x - 4M\omega_d{}^2\right)^2 + 4c^2\omega_d{}^2}}$$

$$-\frac{\xi\frac{\partial C}{\partial x}V_cV_d\cos(\omega_c t + \omega_d t - \phi_6)}{2\sqrt{\left(k_x - M(\omega_c + \omega_d)^2\right)^2 + c^2(\omega_c + \omega_d)^2}}$$

here

$$\phi_1 = \arctan(\frac{\omega_d c}{k_x - M\omega_d{}^2}), \phi_2 = \arctan(\frac{\omega_c c}{k_x - M\omega_c{}^2})$$

$$\phi_3 = \arctan(\frac{2\omega_d c}{k_x - 4M\omega_d{}^2}), \phi_4 = \arctan(\frac{2\omega_c c}{k_x - 4M\omega_c{}^2}) \qquad (3)$$

$$\phi_5 = \arctan(\frac{c(\omega_c - \omega_d)}{k_x - M(\omega_c - \omega_d)^2})$$

$$\phi_6 = \arctan(\frac{c(\omega_c + \omega_d)}{k_x - M(\omega_c + \omega_d)^2})$$

The current at the sense electrode has three components: motion induced current i_m, capacitive current due to voltage change i_c and parasitic current.

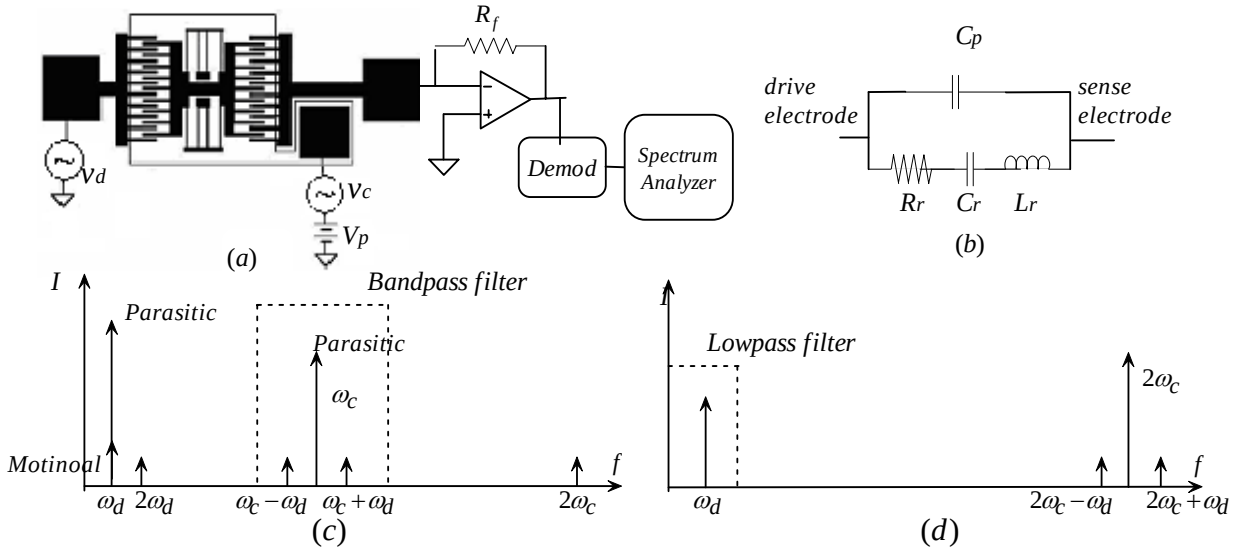

Fig 6: a) Schematic of mixing frequency measurement for spectrum analysis; b) equivalent circuit of the resonator shown in a); c) current spectrum at the sensing electrode; d) the spectrum after demodulation

The first two currents can be expressed as:

$$i_s = \frac{\partial[\xi C v(t)]}{\partial t} = \xi C \frac{\partial v(t)}{\partial t} + \xi v(t) \frac{\partial C}{\partial x}\frac{\partial x}{\partial t} = i_c + i_m \quad (4)$$

where $v(t)$ is the bias voltage between the structure and the sensing electrode and equals to the sum of V_p and v_c. The parasitic current is:

$$i_p = C_p \frac{dv}{dt} \quad (5)$$

By carefully choosing the carrier, the resonance can be excited only by $v_d(t)$. Using equation (3) and (4) to solve the lower side band of motional current at resonance, $i_{m,lsb}$ may be expressed as:

$$i_{m,lsb} = v(t)\xi\frac{\partial C}{\partial x}\frac{\partial x}{\partial t} = \xi^2\left(\partial C/\partial x\right)^2 \frac{V_p V_d V_c}{2}\sqrt{A^2+B^2}\,Sin[(\omega_c-\omega_d)t+\varphi] \quad (6)$$

where

$$A = \frac{\omega_d(k_x - M\omega_d^2)}{(k_x - M\omega_d^2)^2 + c^2\omega_d^2} - \frac{(\omega_c-\omega_d)(k_x - M(\omega_c-\omega_d)^2)}{(k_x - M(\omega_c-\omega_d)^2)^2 + c^2(\omega_c-\omega_d)^2} \quad (7)$$

$$B = \frac{c\omega_d^2}{(k_x - M\omega_d^2)^2 + c^2\omega_d^2} + \frac{c(\omega_c-\omega_d)^2}{(k_x - M(\omega_c-\omega_d)^2)^2 + c^2(\omega_c-\omega_d)^2} \quad (8)$$

$$\varphi = \arctan\left(\frac{B}{A}\right) \quad (9)$$

Alternatively, if we define $C = \xi(C_0 + C_m\cos\omega t)$, where C_0 is the static finger-to-finger overlap capacitance and C_m is the capacitance occurred at the maximum displacement, the lower side band of the motional current in terms of C_m can be expressed as:

$$i_{m,lsb} = \left(\xi v(t)\frac{dC}{dt}\right)_{lsb} = -\frac{1}{2}\xi C_m \omega_d V_c \cos(\omega_c - \omega_d)t \quad (10)$$

Comparing equation (6) and (10), C_m can be expressed in phasor form:

$$C_m = V_p V_d \xi\left(\partial C/\partial x\right)^2 \frac{\sqrt{A^2+B^2}}{\omega_d}\angle(\varphi + 90^\circ) \quad (11)$$

Solving equation (4) at resonance in terms of C_m, the output of the bandpass filter i_0 can be expressed as:

$$i_0 = \xi C_0 \omega_c V_c \cos(\omega_c t) + \tfrac{1}{2}\cdot\xi C_m V_c(\omega_c - \omega_d)\cos(\omega_c t - \omega_d t) + \tfrac{1}{2}\cdot\xi C_m V_c(\omega_c + \omega_d)\cos(\omega_c t + \omega_d t) \quad (12)$$

Demodulation can be achieved by multiplying i_0 by an effective multiplier $R\sin(\omega_c t + \theta)$, where R is determined by the transmittance amplifier and the effective gain of Gilbert cell multiplier [11]. The output of the "Demod" box is:

$$V_o = \frac{1}{2}\xi C_m V_c R\sqrt{(\omega_c\sin\theta)^2 + (\omega_d\cos\theta)^2}\angle\arctan\left(-\frac{\omega_d\cos\theta}{\omega_c\sin\theta}\right) \quad (13)$$

To maximize the output voltage at resonance, the multiplier should be chosen with $\theta = 90^{\circ}$, a phase shifter is need for this purpose. Thus V_o becomes:

$$V_o = \frac{1}{2}\xi^2 V_p V_d V_c R\left(\partial C/\partial x\right)^2 \frac{\omega_c\sqrt{A^2+B^2}}{\omega_d}\angle(\varphi+90^{\circ}) \quad (14)$$

where $\partial C/\partial x$ can be obtained from references [6] and [14]. If the amplitude of the applied voltages and R are fixed, thus $0.5V_pV_dV_cR\xi^2\cdot(\partial C/\partial x)^2$ can be regarded as a constant and is independent of frequency. If spectrum is expressed in decibels, then $(\omega_c/\omega_d)(\sqrt{A^2+B^2})dB$ can fully characterize the system, while the spectrum should shift downward according to $0.5V_pV_dV_cR\xi^2\cdot(\partial C/\partial x)^2 dB$.

Using the system specifications listed in Table 1, the plot of $(\omega_c/\omega_d)(\sqrt{A^2+B^2})dB$ is shown Fig. 7.a. The quality factor may be calculated using the –3dB bandwidth:

$$Q = \frac{f_r}{f_2 - f_1} = \frac{f_0}{f_2 - f_1} \approx \frac{16964}{17283-16643} = 26.5 \quad (15)$$

which is in the range which is reported for comb drive operating at air pressure [6],[8]. Fig 7.b compares the frequency response of the system operating in two levels of vacuum with damping coefficients of $1e-7$ and $1.4e-8$ with atmospheric pressure. Fig.7.c indicates the frequency response for systems with different spring constants, $0.58N/m$, $1.16N/m$ and $1.74N/m$ from left to right.

TABLE 1: System Parameters

Effective mass	$5.4568\times10^{-11}kg$
Spring constant	$0.62N/m$
Damping coefficient	2.2×10^{-7}
Carrier frequency	100 kHz

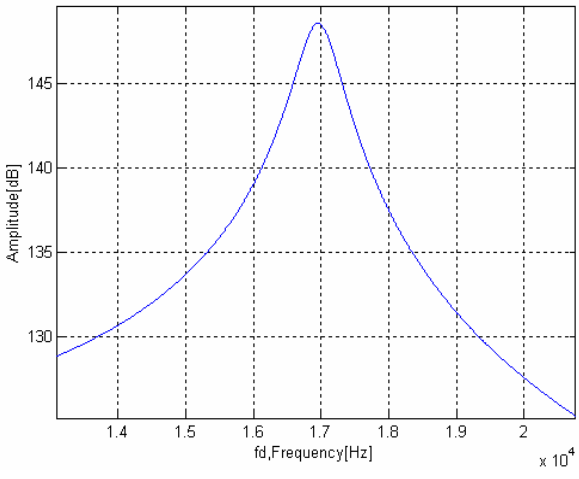

a

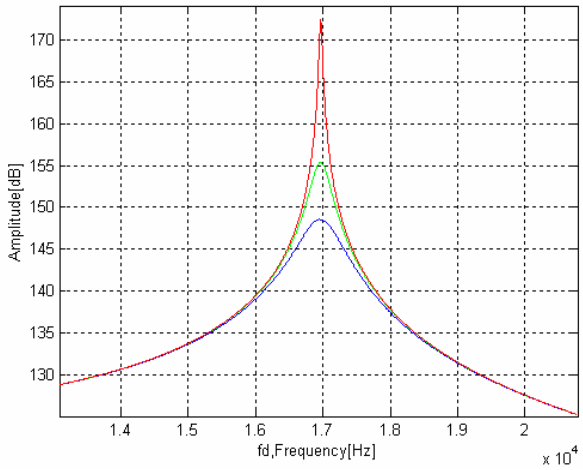

b

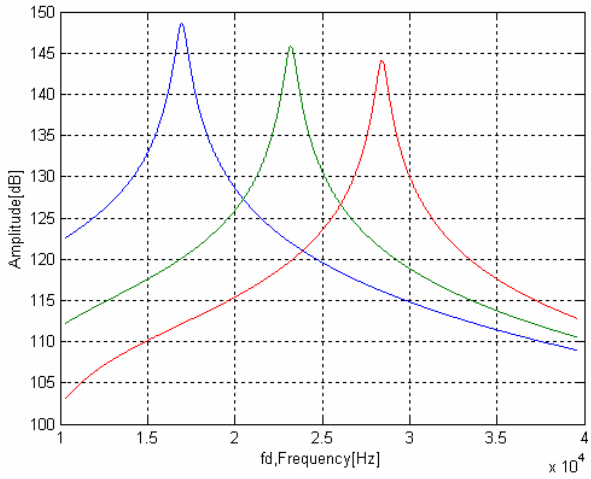

c

Fig. 7. a) Plot of frequency response at atmospheric pressure; b) comparison of spectrum operating at different pressures; c) comparison of spectrum with different spring constants.

Frequency doubling might be used to eliminate the effect of feedthrough, by allowing signal frequency to be half of the resonant frequency. However the harmonic distortion in the output signal of a signal generator makes the frequency doubling measurement difficult. The harmonic distortion is caused by the presence of frequencies that are not in the input signal. These frequencies are usually a sinusoidal component of a periodic wave or quantity having a frequency that is an integral multiple of the fundamental frequency. The harmonic distortion at $2\omega_d$ will induce feedthrough current, which may mask the motional current.

Experimental results

Direct observation in SEM (scanning electron micrograph) is carried out first to find out the resonant

mode and resonant frequency. The SEM acceleration voltage is limited to about 1.6kV to minimize charging from the scanning electron beams [6]. Subsequent spectrum measurement in air is made via the mixing frequency method. The frequency domain technique converts time domain data into discrete frequency components using a fast Fourier transform. Because most machine-train failures results at or near a frequency component associated with the running speed, spectrum analysis is extremely important to characterize the system.

TABLE 2: Unbalanced Comb Drive Parameters

Parameter	Value
Folded-Beam Length	200 μm
Folded-Beam Width	2 μm
Structural Layer Thickness	2 μm
Number of Fingers	14 (left), 12 (right)
Finger Length	40 μm
Finger Width	3 μm
Finger Gap Spacing	2 μm
Finger engagement	20 μm
Width of Cantilever Beam	13 μm
Length of Cantilever Beam	80 μm
Young's Modulus [10]	160-180Gpa
Effective Mass	$5.4568\times10^{-11} kg$
System Spring Constant	$0.62 N/m$
Predicted Resonant Frequency	16964 Hz

Table 2 lists the fabricated unbalanced comb drive parameters used for SEM observation, in which the effective mass is calculated under the assumption that there is no offset and sidewall angle of polysilicon devices fabricated by the Multi-User MEMS Processes. The resonant frequency without the effect of process offset is calculated by equation (1), choosing 160 GPa as Young's modulus. The resonant frequency including the effects of a distributed mass, residual stress, and compliant support could be determined by means of the analytical model proposed in [12].

Fig. 8 is the erratic SEM observation of the unbalanced comb drive at resonance, with DC voltage applied to the resonator and AC signal applied to the drive electrode. The resonance is determined when the displacement amplitude reaches maximum while frequency sweeping upwards. The lower set of fingers is from drive electrode and is fixed and the lateral displacement of the resonator (the upper set of fingers) is approximately 3.5 μm . The wave propagation along the upper fingers indicates the rotation due to asymmetry. The direction of the rotation axis is along the length of folded-beams. The simulated mode shape in ANSYS is illustrated in Fig. 9. The displacement contour plot in Z direction (perpendicular to the substrate) at lateral resonant mode indicates the rotation due to the asymmetry.

The same device is used for mixing frequency measurement using circuit in Fig. 6.a and the complete schematic for the circuit within the "Demod" box is described in [11]. The frequency spectrum is shown in Fig 10. The erratic side bands indicate the rotation frequency component and the impact between movable structure and shielding. The spectrum indicates a loss of stability and system failure may results at those sidebands. The range of instability varied for different resonators and voltage applied, nevertheless, for the tested unbalanced comb drive, erratic behaviour could be induced at some value or range of frequencies.

The balanced comb drive with the same cantilever attached on the left side has the same parameters as those in Table 2. No erratic observation is found in SEM measurements and the device operates in pure lateral.

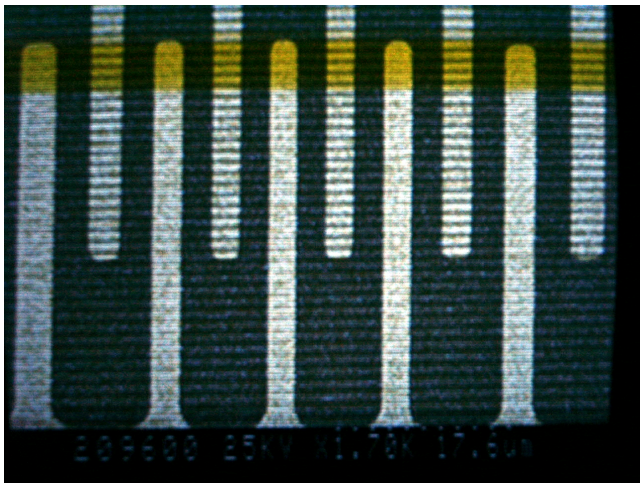

Fig. 8. Direct SEM observation of unbalanced comb drive with a cantilever attached

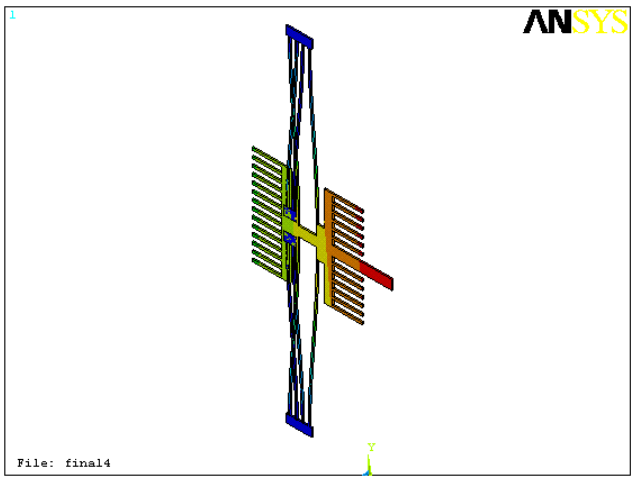

Fig. 9. Displacement contour plot in Z direction at lateral resonant mode

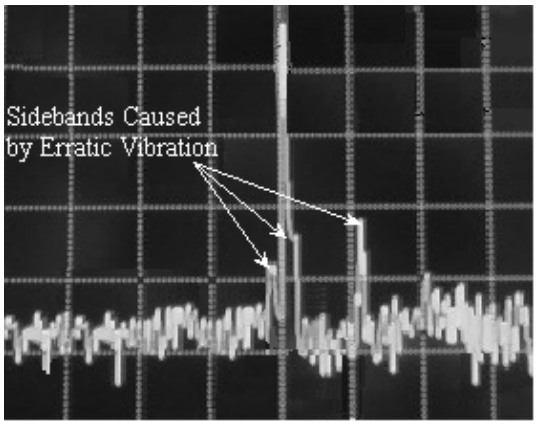

Fig. 10. Output spectrum for unbalanced comb drive, measured at air pressure. (Y-axis: 5 dB/div and X-axis: 5 kHz/div)

resonant mode. The resonant frequency is 17620 Hz, which is slightly larger than the predicted value listed in Table 2, indicating that a higher Young's modulus should be used. For balanced comb drive measured with mixing frequency method, the spectrum is given in Fig. 11 and the quality factor is around 29.

$$Q \approx \frac{17.6}{17.9-17.3} \approx 29$$

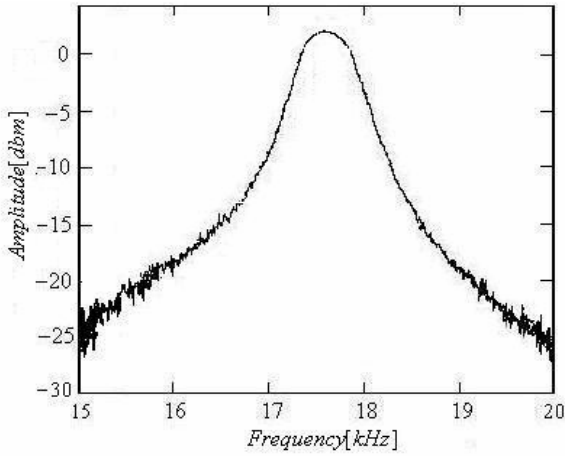

Fig. 11. Output spectrum for balanced comb drive measured at air pressure

Conclusion

In this paper, we have discussed several issues of balanced and unbalanced comb drives including resonant modes, mechanism of lateral displacement and vertical levitation as well as the fringing field effect, which helps to actuate the comb drive. Theoretical expressions governing the spectrum are derived. Unbalanced and balanced comb drives are tested in the same configuration. The unbalanced comb drive presents instability in both SEM observations and spectrum analysis, while balanced comb drive eliminate rotational motion and significantly improves the stability.

Acknowledgement

The authors would like to acknowledge Canadian Microelectronics Corporation (CMC), National Sciences and Engineering Research Council of CANADA (NSERC) and Faculty of Electrical & Computer Engineering at Concordia University for their invaluable support of this project.

Reference

[1] Long-Sheneg Fan, Yu-Chong Tai, and Muller,R.S, "IC-processed electrostatic micro-motors", *Electron Devices Meeting, 1988, Technical Digest, International* 11-14 Dec, 1988, pp:666-669.

[2] Tai,Y.-C, Fan,L-S, Muller,R.S, "IC-processed micromotors: design, technology, and testing", *Micro Electro Mechanical Systems, 1989, Proceedings, 'An Investigation of Micro Structures, Sensors, Actuators, Machines and Robots'. IEEE* , 20-22 Feb. 1989, pp:1 – 6.

[3] Ernest J. Garcia, Jeffry J. Sniegowski, "Surface Micromachined microengine", *Sensors and Actuators A* 48 (1995) 203-214.

[4] Rob Legtenberg, Erwin Berenschot, Miko Elwenspoek, and Jan H. Fluitman, "A Fabrication Process for Electrostatic Microactuators with Integrated Gear Linkages", *Journal of Microelectromechanical Systems*, Vol.6, No.3, Sep,1997.

[5] W.-H. Juan and S.W. Pang, "High-Aspect-Ratio Si Vertical Micromirror Arrays for Optical Switching", *Journal of Microelectromechanical Systems*, Vol. 7, No. 2, June 1998.

[6] W.C.Tang, *"Electrostatic comb drive for resonant sensor and actuator applications"*; Ph.D dissertation, Univ. California Berkeley, Berkeley, CA, 1990.

[7] William C.Tang, Martin, G.Lim and Roger T. Howe; "ELECTROSTATICALLY BALANCED COMB DRIVE FOR CONTROLLED LEVITATION", *Tech. Digest, IEEE Solid-State Sensor and Actuator Workshop*, June 1990, pp23-27.

[8,] W.C.Tang, T.-C.H.Nguyen, and R.T.Howe, "Laterally driven polysilicon resonant microstructures", *Sensors and Actuators*, vol 20, pp25-32, 1989.

[9] William C.Tang, Martin, G.Lim and Roger T.Howe; "Electrostatic Comb Drive Levitation and Control Method", *Journal of Microelectromechanical System*, vol.1, No.4, December 1992.

[10]David A.Koester, Ramaswamy Mahadevan, Busbee Hardy and Karen W. Markus, *MUMPSs Design Handbook, Revision 7.0*, Cornos Integrated Microsystems, A JDS Uniphase Company, Research Triangle Park, NC 27709.

[11] Jun Cao and Clark T.-C. Nguyen; "Drive Amplitude Dependence of Micromechanical Resonator Series Motional Resistance"; *Digest of Technical Papers, 10th International Conference on Solid-State Sensors and Acturtors*, Sendai, Japan, June 7-10, 1999, pp1826-1829.

[12] Raj K. Gupta, "Electronically Probed Measurements of MEMS Geometries", *Jounal of Microelectromechanical Systems*, Vol 9, No.3, September 2000.